Cascade-Dissipation Balance in Astrophysical Plasmas: Insights from the Terrestrial Magnetosheath

D. Manzini,[1,2,*] F. Sahraoui,[1] and F. Califano[2]

[1]Laboratoire de Physique des Plasmas (LPP), CNRS, École Polytechnique, Sorbonne Université, Université Paris-Saclay, Observatoire de Paris, 91120 Palaiseau, France

[2]Dipartimento di Fisica E. Fermi, University of Pisa, Italy

(Received 14 December 2023; revised 28 March 2024; accepted 2 May 2024; published 4 June 2024)

The differential heating of electrons and ions by turbulence in weakly collisional magnetized plasmas and the scales at which such energy dissipation is most effective are still debated. Using a large data sample measured in Earth's magnetosheath by the magnetospheric multiscale mission and the coarse-grained energy equations derived from the Vlasov-Maxwell system, we find evidence of a balance over two decades in scales between the energy cascade and dissipation rates. The decline of the cascade rate at kinetic scales (in contrast with a constant one in the inertial range), is balanced by an increasing ion and electron heating rates, estimated via the pressure strain. Ion scales are found to contribute most effectively to ion heating, while electron heating originates from both ion and electron scales. These results can potentially impact the current understanding of particle heating in turbulent magnetized plasmas as well as their theoretical and numerical modeling.

DOI: 10.1103/PhysRevLett.132.235201

One of the central problems in turbulent media is to understand how energy is transferred across scales and how it is eventually dissipated. For weakly collisional plasma such as the solar wind or planetary magnetosheaths, the pioneering work of Politano and Pouquet [1] enables us, in the framework of incompressible magnetohydrodynamics (MHD) and under the assumptions of fully developed turbulence, to express the cascade rate as a function of third order structure functions of the velocity and magnetic field [2]. These results have been extended to account for compressibility [3,4], the contribution of the Hall current at subion scales [5–7], different fluid closure equations [8] and temperature anisotropy [9] and have been used extensively to measure the cascade rate in spacecraft data [10–23]. In recent years the coarse-graining (CG) method, initially developed for hydrodynamics [24,25], gained popularity in the plasma physics community [26–30]. This formulation provides an alternative way to measure the cascade rate and enables us to overcome some limitations imposed by the stringent hypotheses of fully developed turbulence (e.g., spatial homogeneity). Indeed, the CG approach can be employed not only to measure the average cascade rate over large plasma portions but also to address localized cross-scale energy transfer in reconnecting current sheets [31,32]. In this work we scale filter the Vlasov-Maxwell equations and measure the nonlinear energy cascade rate and the exchanges between its various forms (kinetic, electromagnetic and "thermal," defined below) as a function of scale, with a particular focus on the turbulent plasma heating given by the pressure-strain interaction [33,34].

The coarse graining theory.—To study cross-scale energy transfer we apply the spatial CG approach to the moments of the Vlasov equation, written for an electron-ion plasma ($\alpha = e, i$), and the Maxwell ones. All variables are low-pass filtered at a scale ℓ, e.g., $\bar{\mathbf{v}}_\ell = \int d\boldsymbol{r} G_\ell(\boldsymbol{r})\mathbf{v}(\boldsymbol{x}+\boldsymbol{r})$, where G_ℓ is a centered, normalized filtering kernel with variance of order ℓ^2 [35]. To include the effects of compressibility we introduce a density-weighted filtering (*Favre filtering*) defined for a given field f as $\tilde{f}_\ell = \overline{\rho f}_\ell/\bar{\rho}_\ell$ [36,37]. For conciseness of the notations the filtering scale ℓ is not written explicitly unless necessary.

At each scale ℓ we can write the equations for the large-scale bulk flow ($\tilde{\mathcal{E}}^{\mathrm{f}}_\alpha = \overline{\rho_\alpha}|\tilde{\mathbf{v}}_\alpha|^2/2$), electromagnetic [EM, $\bar{\mathcal{E}}^{\mathrm{em}} = (|\bar{\boldsymbol{E}}|^2 + |\bar{\boldsymbol{B}}|^2)/8\pi$] and thermal energies [$\bar{\mathcal{E}}^{\mathrm{th}}_\alpha = \mathrm{Tr}(\overline{\boldsymbol{P}_\alpha})/2$]:

$$\frac{\partial}{\partial t}(\tilde{\mathcal{E}}^{\mathrm{f}}_i + \tilde{\mathcal{E}}^{\mathrm{f}}_e) = -\nabla\cdot\boldsymbol{\mathcal{F}}^{\mathrm{f}}_\ell + \bar{\boldsymbol{j}}\cdot\bar{\boldsymbol{E}} + \bar{\boldsymbol{P}}_i : \nabla\bar{\mathbf{v}}_i + \bar{\boldsymbol{P}}_e : \nabla\bar{\mathbf{v}}_e - \pi(x,\ell) \tag{1}$$

$$\frac{\partial}{\partial t}\bar{\mathcal{E}}^{\mathrm{em}} = -\nabla\cdot\boldsymbol{\mathcal{F}}^{\mathrm{em}}_\ell - \bar{\boldsymbol{j}}\cdot\bar{\boldsymbol{E}} \tag{2}$$

$$\frac{\partial}{\partial t}\bar{\mathcal{E}}^{\mathrm{th}}_\alpha = -\nabla\cdot\boldsymbol{\mathcal{F}}^{\mathrm{th}}_\ell - \nabla\cdot\bar{\mathbf{h}}_\alpha - \overline{\boldsymbol{P}_\alpha} : \nabla\overline{\mathbf{v}_\alpha} - \phi_\alpha(x,\ell), \tag{3}$$

where

$$\pi(x,\ell) = \sum_{\alpha=e,i} -\overline{\rho_\alpha}[\widetilde{\mathbf{v}_\alpha\mathbf{v}_\alpha} - \widetilde{\mathbf{v}}_\alpha\widetilde{\mathbf{v}}_\alpha] : \nabla\widetilde{\mathbf{v}}_\alpha + (\nabla\overline{\boldsymbol{P}_\alpha})\cdot(\widetilde{\mathbf{v}}_\alpha - \overline{\mathbf{v}_\alpha}) - \overline{n_\alpha q_\alpha \mathbf{v}_\alpha}\cdot\left[(\tilde{\boldsymbol{E}} - \overline{\boldsymbol{E}}) + \frac{1}{c}\left(\widetilde{\mathbf{v}_\alpha\times\boldsymbol{B}} - \widetilde{\mathbf{v}}_\alpha\times\tilde{\boldsymbol{B}}\right)\right] \quad (4)$$

is the cross-scale energy transfer (or *turbulent cascade*) rate across the scale ℓ. The quantities $\bar{\boldsymbol{j}}\cdot\bar{\boldsymbol{E}}$ and $\mathrm{PS}_\alpha \equiv \overline{\boldsymbol{P}_\alpha} : \nabla\overline{\mathbf{v}_\alpha}$ are the only sink terms of the large-scale EM and thermal energy, respectively, and appear as a source in the large scale bulk flow energy. This implies that any process that changes the large-scale thermal energy must go through the PS_α channel. At the same time Eq. (1) shows that (a fraction of) $\boldsymbol{j}\cdot\boldsymbol{E}$ can lead to plasma heating (via the PS_α) without having to modify the large scale bulk flow energy. This can be seen even more clearly by summing equations (1) and (3), which indicates that $\boldsymbol{j}\cdot\boldsymbol{E}$ acts as a source for the total kinetic energy of the plasma particles (bulk flow *and* thermal energy) [38]. The quantity $\phi_\alpha = \overline{\boldsymbol{P}_\alpha : \nabla\mathbf{v}_\alpha} - \overline{\boldsymbol{P}_\alpha} : \nabla\overline{\mathbf{v}_\alpha}$ stands for a nonlinear cascade of thermal energy. This term transfers thermal energy from large to small spatial scales and will not be discussed in this work since we only consider transfer *to* the thermal energy and not how this quantity rearranges itself over scales. While $\bar{\boldsymbol{j}}\cdot\bar{\boldsymbol{E}}$ and $\overline{\boldsymbol{P}_\alpha} : \nabla\overline{\mathbf{v}_\alpha}$ are cumulative quantities, encompassing the energy exchanges from all scales larger than ℓ, the cross-scale terms π, ϕ measure the transfer *across* scale ℓ. The spatial fluxes in the form $\nabla\cdot\boldsymbol{\mathcal{F}}$, including the divergence of the filtered heat flux $\nabla\cdot\overline{\mathbf{h}_\alpha}$, move the large scale energies in space and disappear after integration over a suitable domain. The full derivation of these equations and the expression of the spatial fluxes can be found in Appendix A together with a discussion of the difference between Eqs. (1)–(3) and those derived in Yang *et al.* [29]. Summing Eqs. (1)–(2) and averaging over a portion of plasma yields

$$\frac{\partial}{\partial t}\left\langle \tilde{\mathcal{E}}_i^{\mathrm{f}} + \tilde{\mathcal{E}}_e^{\mathrm{f}} + \bar{\mathcal{E}}^{em}\right\rangle + \nabla\cdot\left\langle \boldsymbol{\mathcal{F}}_\ell^{\mathrm{f}} + \boldsymbol{\mathcal{F}}_\ell^{\mathrm{em}}\right\rangle = \mathrm{PS}_i(\ell) + \mathrm{PS}_e(\ell) - \Pi(\ell), \quad (5)$$

where in the right-hand side we find the average PS interaction, $\mathrm{PS}_\alpha(\ell) = \langle\overline{\boldsymbol{P}_\alpha} : \nabla\overline{\mathbf{v}_\alpha}\rangle$, filtered at scale ℓ, and the net energy cascade $\Pi(\ell) = \langle\pi_\ell\rangle$.

Equation (5) states that, under the assumption of suitable boundary conditions, what is lost by the large-scale energies either cascades to smaller scales or is transferred to thermal energy. In this view the pressure-strain interaction plays the role of an energy sink. For this reason we will refer to it as *dissipation*, even if it is somehow inappropriate (see discussion below).

We evaluate Eq. (5) between scales ℓ_0 and $\ell < \ell_0$. Under the hypotheses of negligible spatial fluxes and energy stationarity (or a simple balance between the two) at scales smaller than ℓ_0, we find

$$\Pi(\ell_0) - \Pi(\ell) = -\Delta\mathrm{PS}_i(\ell) - \Delta\mathrm{PS}_e(\ell), \quad (6)$$

where $-\Delta\mathrm{PS}_\alpha(\ell) = -\mathrm{PS}_\alpha(\ell) + \mathrm{PS}_\alpha(\ell_0)$ is the cumulative contribution to the heating rate of species α in the range $[\ell, \ell_0]$. Equation (6) shows that any difference between $\Pi(\ell_0)$ and $\Pi(\ell)$ will reflect the amount of energy that is lost to thermal energy between those two scales. In this perspective, a constant cascade rate indicates an *inertial range* where dissipation is negligible, while a scale-dependent cascade rate is the signature of active dissipation. It must be stressed that relation (5) comes directly from the Vlasov-Maxwell equations, and as such is not limited by any fluid approximation since no closure equation is imposed on the pressure. This implies that if kinetic effects play a role in heating the plasma, this will be captured by the PS interaction, which explains why the energy cascade rate (inherently a fluid quantity) could capture dissipation via Landau damping in turbulence simulations [39]. However, the interpretation of PS as a measure of change in the thermal energy (i.e., heating) is grounded on the assumption that the spatial fluxes contribution $\nabla\cdot\langle\mathcal{F}_\ell^{\mathrm{th}} + \overline{\mathbf{h}_\alpha}\rangle$ in Eq. (3) are negligible. Notice that this condition applies to averaged filtered fields and not to local (pointwise) quantities.

Data selection and methods.—We use data from the magnetospheric multispacecraft (MMS) mission [40], which enables us to compute the spatial derivatives in PS_α and Π using the gradiometer technique [41]. We use FluxGate magnetometer data for the magnetic field, the spin-plane double probe [42] and the axial double probe [43] for the electric field and the fast plasma investigation [44] for the plasma data. Spin-tone removal is applied to the electron velocity data [45]. The CG operation in spacecraft data at a given timescale τ is computed as $\bar{f}_\tau(t) = \int dt' G_\tau(t') f(t+t')$, where G_τ is a one-dimensional Gaussian kernel with variance $\tau^2/4$: $G_\tau(t) = e^{-2t^2/\tau^2}/\sqrt{\pi\tau^2/2}$. The timescale τ is related to the spatial scale ℓ via the mean flow speed $\ell \sim \tau V_f \sim 1/k$ using the Taylor hypothesis. To minimize the finite sample size effect, the maximum scale $\tau_{\max}$ should be significantly smaller than the duration of the interval under consideration. The smallest accessible scale $\tau_{\min}$ is constrained by the instrument time resolution (typically 150 ms for ions); we set $\tau_{\min}$ at twice this value. When combining MMS products of different time resolutions, we resample the data at the frequency of the least resolved quantity. It is worth noting that the electron contributions to the cascade rate and PS_e do not involve ion data, and as such they are computed down to (twice) the electron data time resolution of 30 ms.

To ensure the robustness of the results with respect to the choice of the start and final time of each interval we follow this pipeline: we compute $\pi, \overline{P_i} : \nabla\overline{v_i}, \overline{P_e} : \nabla\overline{v_e}$ for all the data points in the interval $[t_{\mathrm{start}}, t_{\mathrm{end}}]$. We then average

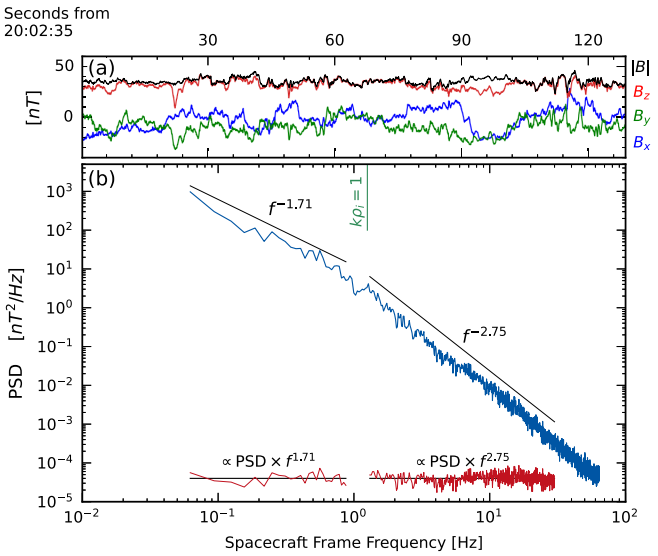

FIG. 1. Panel (a) shows the time series of the magnetic field measured by MMS3 in geocentric solar ecliptic (GSE) coordinates. Panel (b) displays the power spectrum of the magnetic field data computed using the Welch method [47]. Power-law fit and compensated spectra are shown. Time series for other relevant quantities are shown in Fig. 7.

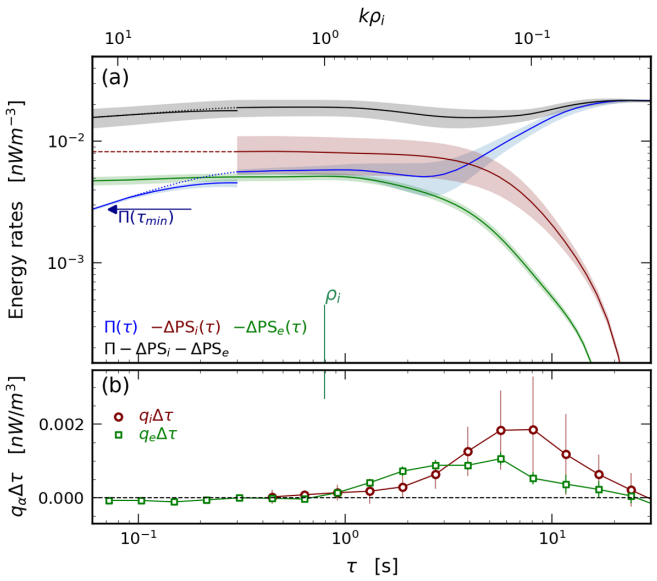

FIG. 2. Panel (a) shows the different terms of Eq. (6) as a function of τ and $k\rho_i$ (top axis) for the interval shown in Fig. 1. Shaded regions denote the error bars. At time lags smaller than the time resolution of the ion data we assume that there is no additional contribution to ion heating [hence a constant $\Delta PS_i(\tau)$, dashed], moreover only the electron contribution to the cascade is computed. The dotted lines are a cubic spline interpolation to aid the visualization. Panel (b) shows the scale dependent ion and electron heating rates (see text).

the above quantities in an interval $[t_{\rm start} + \Delta t_1, t_{\rm end} - \Delta t_2]$. By varying independently $\Delta t_1, \Delta t_2$ between 0% and 10% of the interval duration we obtain different estimates of the cascade rate Π and PS_α. At each scale, we take the median value as our best estimate and use the median absolute deviation as the error bar estimate. A different method (not shown) based on propagating the estimated error of the FPI measurements [46] yields smaller or comparable uncertainties to those obtained here with the above empirical method.

Results.—We show in Fig. 1 and in Fig. 7 the data from MMS3 taken in Earth's magnetosheath (2016/02/23, 20:02:35–20:04:44). During this time the average plasma conditions were $B \approx 35$ nT, $n_e \approx 19$ cm^{-3}, $T_i \approx 175$ eV $T_e \approx 27$ eV. The ratio of thermal to magnetic pressure is $\beta_i \approx 1.07, \beta_e \approx 0.16$. The mean flow speed $V_f \approx 300$ km/s and the angle between the flow and the magnetic field $\theta_{\mathbf{vB}} \approx 100^o$. The interspacecraft separation is of ∼11 km. The magnetic field power spectrum (Fig. 1) displays a $f^{-1.7}$ scaling in the MHD range and steepens to $f^{-2.75}$ at higher frequencies.

Figure 2(a) shows the balance between the energy cascade rate Π and the dissipation rate as a function of scale τ. At large scales, within the inertial range, the dominant process is the cascade, while at smaller scales, approaching $\tau \sim 4$ s ($k\rho_i \sim 0.2$), dissipation grows and the turbulent cascade is progressively weakened. Following Eq. (6), the decline in the cascade rate is counterbalanced by a rise in the ion and electron PS, maintaining the sum of the three quantities constant over two decades of scales.

Figure 2(a) shows that the small-scale edge of the MHD range is highly dissipative as the cascade rate weakens by a factor ∼4, consistent with the idea of increased dissipation around the spectral break [48]. Throughout the weakly dissipative subion range the cascade rate keeps weakening progressively.

From the behavior of quantities $\Delta\mathrm{PS}_\alpha$ it is not immediate to infer at which scales ions and electrons are heated most. PS_α being a cumulative quantity, the contribution to the heating rate of a given scale range $(\tau,\tau+\Delta\tau)$ is simply $-\mathrm{PS}_\alpha(\tau) + \mathrm{PS}_\alpha(\tau+\Delta\tau) \approx -(\partial \mathrm{PS}_\alpha/\partial\tau)\Delta\tau \equiv q_\alpha(\tau)\Delta\tau$, which is the quantity plotted in Fig. 2(b) after binning logarithmically the range of scales.

The total heating rate for each species is defined as $Q_\alpha = \int_{\tau_{\rm min}}^{\tau_{\rm max}} q_\alpha(\tau)d\tau = \mathrm{PS}_\alpha(\tau_{\rm max}) - \mathrm{PS}_\alpha(\tau_{\rm min})$, $\tau_{\rm min} = 0.3$ s (0.06 s) for ions (electrons) is twice the plasma data resolution and $\tau_{\rm max} = 30$ s for this interval. For ions we obtain a total heating rate $Q_i = (8 \pm 3) \times 10^{-3}$ nW/m^3 (assuming no additional contribution to ion heating originates from scales smaller than 0.3 s). For electrons, we estimate the heating rate Q_e similarly to ions. However, that quantity is complemented by an extra term given by the energy cascade rate at the smallest available time lag, namely $\Pi(\tau = \tau_{\rm min})$ [highlighted in Fig. 2(a) for $\tau_{\rm min} \sim 0.06$ s], i.e., $Q_e^\star = Q_e + \Pi(\tau_{\rm min})$. This is based on the assumption that the residual cascade rate $\Pi(\tau_{\rm min})$ will be entirely converted

into electron heating at the smallest scales. Thus, we obtain the value $Q_e^\star = (7.5 \pm 0.4) \times 10^{-3}$ nW/m^3 for the total electron heating rate. The cascade rate at MHD scales has a value of $\Pi(\tau_{\max}) = (2.1 \pm 0.1) \times 10^{-2}$ nW/m^3 placing the ratio $\Pi(\tau_{\max})/(Q_i + Q_e^\star) \simeq 1$. We thus verify Eq. (6): the cascading energy has been converted to thermal energy via the PS. This observation confirms previous numerical results where the balance between the cascade rate and dissipation via PS was first reported [29,48,49] and improves over the comparison between PS and the cascade rate estimate via incompressible third order laws presented in [50].

The study of the scale-dependent heating rate $q_\alpha(\tau)\Delta\tau$ informs us about the scales most effective in heating the two species. Figure 2(b) shows that the largest contribution to ion heating comes from $\tau \approx 8$ s ($k\rho_i \approx 0.1$), in the same range of scales electrons are substantially heated. The residual cascade rate at $\tau_{\min} = 0.06$ s, assumed to sustain the turbulence and eventually heat electrons at scales $k\rho_i \gtrsim 13$ [51], accounts for $\Pi(\tau_{\min})/Q_e^\star \sim 35\%$ of the total electron heating rate.

Statistics.—To confirm the statistical robustness of the previous results we perform the same analysis for a large set of MMS intervals taken in the magnetosheath. The selection criteria of the data intervals are given in Appendix B together with additional details of the dataset. We further narrowed down the selection to keep only data intervals that satisfy (within the error bars) the energy balance defined by $\Pi(\tau_{\max})/(Q_i + Q_e^\star) \in [0.4, 1.6]$ to ensure that spatial fluxes and time derivatives in Eq. (5) are negligible in the range of scales we are considering. This guarantees a reliable estimation of the cascade rate, the ion and electron heating rates, and the related effective dissipation scales. Out of the 84 intervals studied, 39 satisfy the strict balance condition imposed, showing that relation (6) is reasonably satisfied (to order unity) in the magnetosheath. To increase the size of the statistical sample, for a given interval we consider each spacecraft as an independent realization, although the spatial derivatives (but not other quantities) involved in Eq. (6) are computed from the four spacecraft and thus are identical for a given event, obtaining a total of 70 events that satisfy the balance condition, summarized in Fig. 3. For these events we show in Appendix C the values of the cascade rate at different scales.

We now wish to delineate the scales at which the PS interaction is effective in heating the plasma. For each species, we calculate the fraction of heating coming from the MHD range ($k\rho_i < 0.5$), around the ion Larmor scale ($0.5 < k\rho_i < 2$) and the subion range ($k\rho_i > 2$). The results in Figs. 4(a)–4(c) show that the largest contribution to the ion heating rate comes from MHD scales (the median contribution being 60%). The relative importance decreases to 30% at the ion Larmor scale and then <10% at sub-Larmor scales. This result corroborates the assumption made above that the residual cascade at $k\rho_i \gtrsim 10$ translates predominantly into electron heating.

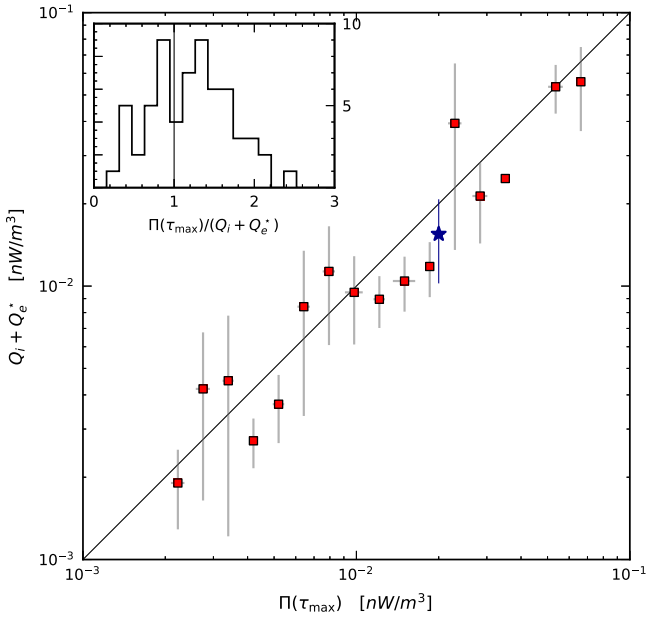

FIG. 3. Cascade-dissipation balance for the selected intervals that satisfy the balance condition (see text) binned according to the value of the cascade rate $\Pi(\tau_{\max})$. The star denotes the case study presented in the text. The inset shows the histogram of the cascade-dissipation ratio for all the intervals that respect (within the error bars) the balance condition.

The picture that emerges for electrons is more complex: even if the subion range holds the largest median contribution (70%), a significant contribution (30%) comes from the MHD and ion scales.

This result demonstrates that electron heating can be significant at scales comparable with the ion Larmor radius (including the edge of the MHD range) in line with previous numerical results [52,53].

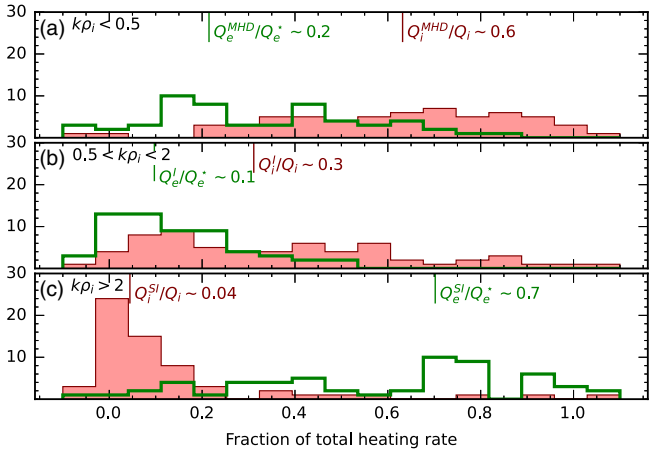

FIG. 4. Histogram of the relative contribution to the heating rate from the three range of scales $k\rho_i < 0.5$ (a), $0.5 < k\rho_i < 2$ (b), $k\rho_i > 2$ (c). Ions (red, solid) and electrons (green, open). In each panel, a vertical sign denotes the median for each population.

Conclusions.—In this work we measure for the first time using *in situ* data the scale dependence of the cascade rate *and* the dissipation rate and show that there exists a balance that holds for over two decades of scales: the weakening of the energy cascade as turbulence proceeds from MHD to kinetic scales is compensated for by a net positive transfer to the thermal energy. On a statistical dataset we show that electrons can get substantial heating at scales comparable with the ion Larmor radius, against the conventional wisdom that electron heating occurs solely at electron scales. This questions the validity of kinetic-hybrid models for plasmas where electrons are treated as a polytropic fluid whose dissipation is confined to the small (electron) resistive scales.

Despite the net decline of the cascade rate in the subion range, the magnetic energy spectra still show clear power laws all the way down to the electron scales ($k\rho_e \lesssim 1$). In the absence of a rigorous explanation for this observation, we speculate that any residual turbulent energy is bound to cascade to small scales following the scaling law of one of the existing modes (e.g., kinetic Alfvén modes [52,54]). Lastly, we mention that identifying PS with dissipation requires some caution, considering that *irreversible* dissipation can only be achieved via a collisional operator that activates when small-scale structures are created in velocity space. In the Vlasov equation used in this work this term is not included, and thus any kinetic process (e.g., Landau damping) is reversible. Therefore, rigorously speaking, the observed heating via PS is simply a reversible exchange with the thermal energy, which can be given back to flow or electromagnetic fluctuations. Nevertheless, the fact that in our dataset we consistently find a net positive heating of the plasma, would imply that the quantity we measure is indeed irreversibly lost to thermal energy in which "collisions" (even if scarce) have certainly played a role. This highlights the need to study directly the velocity distribution functions to asses how the plasma dynamic leads to the creation of small scale structure in velocity space [55–58] as well as identify the underlying kinetic processes responsible for the measured heating [38,59,60].

The PYTHON client SPEASY [61] was used for data retrieval. MMS data come from CDPP/AMDA [62] and NASA GSFC's Space Physics Data Facility's CDAWeb.

D. M. acknowledges useful discussions with A. Chasapis. D. M. and F. S. acknowledge financial support from CNES.

Appendix A: The coarse grained equations.—The CG operation at a given scale ℓ is a convolution, e.g., $\overline{\mathbf{v}}_\ell = \int d\boldsymbol{r} G_\ell(\boldsymbol{r})\mathbf{v}(\boldsymbol{x}+\boldsymbol{r})$, where G_ℓ is a centered, normalized filtering kernel with variance of order ℓ^2. It is a linear operation and it commutes with all derivatives so it can be straightforwardly applied to the moments of the Vlasov equations. In the following, we omit the filtering scale ℓ when there is no risk of ambiguity. Let us consider the filtered continuity and momentum-balance equations:

$$\begin{aligned}
&\partial_t\bar{\rho} + \nabla\cdot(\bar{\rho}\,\tilde{\mathbf{v}}) = 0\\
&\partial_t(\bar{\rho}\,\tilde{\mathbf{v}}) + \nabla\cdot(\bar{\rho}\,\tilde{\mathbf{v}}\,\tilde{\mathbf{v}}) = -\nabla\cdot\bar{\boldsymbol{P}} + q\bar{n}\left[\bar{\boldsymbol{E}} + \frac{(\tilde{\mathbf{v}}\times\tilde{\mathbf{B}})}{c}\right]\\
&\qquad\qquad - \nabla\cdot[\bar{\rho}(\widetilde{\mathbf{v}\mathbf{v}} - \tilde{\mathbf{v}}\,\tilde{\mathbf{v}})] + q\bar{n}(\tilde{\boldsymbol{E}} - \bar{\boldsymbol{E}})\\
&\qquad\qquad + \frac{q\bar{n}}{c}\left(\widetilde{\mathbf{v}\times\mathbf{B}} - \tilde{\mathbf{v}}\times\tilde{\mathbf{B}}\right). \qquad \text{(A1)}
\end{aligned}$$

We recall the *Favre filtering* definition (used above) which enables us to write $\overline{\rho\mathbf{v}}_\ell = \bar{\rho}_\ell\tilde{\mathbf{v}}_\ell$. We stress that the Favre operator is linear but does not commute with derivatives.

The large scale bulk flow kinetic energy is defined as $\widetilde{\mathcal{E}^f} = \frac{1}{2}\overline{\rho}\,\tilde{\mathbf{v}}\cdot\tilde{\mathbf{v}}$. We derive

$$\begin{aligned}
\partial_t\widetilde{\mathcal{E}^f} &= \frac{|\tilde{\mathbf{v}}|^2}{2}\partial_t\overline{\rho} + \bar{\rho}\,\tilde{\mathbf{v}}\cdot\partial_t\tilde{\mathbf{v}}\\
&= \frac{|\tilde{\mathbf{v}}|^2}{2}\partial_t\bar{\rho} + \tilde{\mathbf{v}}\cdot\partial_t(\bar{\rho}\,\tilde{\mathbf{v}}) - |\tilde{\mathbf{v}}|^2\partial_t\bar{\rho}\\
&= \tilde{\mathbf{v}}\partial_t(\bar{\rho}\,\tilde{\mathbf{v}}) + \frac{|\tilde{\mathbf{v}}|^2}{2}\nabla\cdot(\bar{\rho}\,\tilde{\mathbf{v}}). \qquad \text{(A2)}
\end{aligned}$$

Substituting the momentum equation (A1) and rearranging, we find

$$\begin{aligned}
\partial_t\widetilde{\mathcal{E}^f} &= -\nabla\cdot\left[\widetilde{\mathcal{E}^f}\,\tilde{\mathbf{v}} + \overline{\mathbf{v}}\cdot\bar{\boldsymbol{P}} + \bar{\rho}\,\tilde{\mathbf{v}}\cdot(\widetilde{\mathbf{v}\mathbf{v}} - \tilde{\mathbf{v}}\,\tilde{\mathbf{v}})\right]\\
&\quad + \bar{\mathbf{P}}:\nabla\bar{\mathbf{v}} + q\bar{n}\mathbf{v}\cdot\bar{\mathbf{E}}\\
&\quad + \bar{\rho}[\widetilde{\mathbf{v}\mathbf{v}} - \tilde{\mathbf{v}}\,\tilde{\mathbf{v}}]:\nabla\tilde{\mathbf{v}} - (\nabla\bar{\mathbf{P}})\cdot(\tilde{\mathbf{v}} - \bar{\mathbf{v}})\\
&\quad + \overline{nq\mathbf{v}}\cdot\left[(\tilde{\boldsymbol{E}} - \bar{\boldsymbol{E}}) + \frac{1}{c}\left(\widetilde{\mathbf{v}\times\boldsymbol{B}} - \tilde{\mathbf{v}}\times\tilde{\boldsymbol{B}}\right)\right]. \qquad \text{(A3)}
\end{aligned}$$

In the first line we find the spatial flux of large-scale bulk flow energy

$$\boldsymbol{\mathcal{F}}^f_\ell = \bar{\rho}\frac{|\tilde{\mathbf{v}}|^2}{2}\tilde{\mathbf{v}} + \overline{\mathbf{v}}\cdot\bar{\boldsymbol{P}} + \bar{\rho}\,\tilde{\mathbf{v}}\cdot(\widetilde{\mathbf{v}\mathbf{v}} - \tilde{\mathbf{v}}\,\tilde{\mathbf{v}}).$$

The second line contains transfer terms to thermal and electromagnetic energies, namely, the filtered pressure strain and the single species contribution to the filtered $\boldsymbol{j}\cdot\boldsymbol{E}$. The remaining two lines are (minus) the cross-scale energy transfer across scale ℓ (the local cascade rate) of each species.

Notice that if the pressure is isotropic and $\boldsymbol{E} = \boldsymbol{B} = 0$ we recover the expression given by Aluie [37] for compressible hydrodynamics. This was not the case for the equation proposed in Yang *et al.* [29] where the *baropycnal work* $\nabla\boldsymbol{P}\cdot(\tilde{\mathbf{v}} - \bar{\mathbf{v}})$ was not included in the cascade rate.

Moving to the large-scale electromagnetic energy, we filter two of Maxwell's equations:

$$c\nabla\times\bar{\boldsymbol{E}}=-\partial_t\bar{\mathbf{B}}\qquad c\nabla\times\bar{\mathbf{B}}=4\pi\bar{\boldsymbol{j}}-\partial_t\bar{\boldsymbol{E}},\quad\text{(A4)}$$

which can be combined to compute the evolution of the large-scale electromagnetic energy $\bar{\mathcal{E}}^{\rm em}=(|\bar{\boldsymbol{E}}|^2+|\bar{\mathbf{B}}|^2)/8\pi$,

$$\partial_t\bar{\mathcal{E}}^{\rm em}=-\nabla\cdot\left(\frac{c}{4\pi}\bar{\boldsymbol{E}}\times\bar{\mathbf{B}}\right)-\bar{\boldsymbol{j}}\cdot\bar{\boldsymbol{E}},\quad\text{(A5)}$$

where at the right-hand side we find the filtered Poynting flux $\mathcal{F}^{\rm em}_\ell=(c/4\pi)\bar{\boldsymbol{E}}\times\bar{\boldsymbol{B}}$ and the filtered $\boldsymbol{j}\cdot\boldsymbol{E}$. Notice that no cascading mechanism is present in this equation but only the exchange with the plasma. This is to be expected as Maxwell's equations are linear and all the physics of turbulence must be contained in the plasma equations.

Lastly, we write the equation for the thermal energy $\mathcal{E}^{\rm th}=\mathrm{Tr}(\mathbf{P})/2$, which we derive from the second order centered moment of the Vlasov equation

$$\partial_t\mathcal{E}^{\rm th}+\nabla\cdot(\mathbf{v}\mathcal{E}^{\rm th})=-\boldsymbol{P}\colon\nabla\mathbf{v}-\nabla\cdot\mathbf{h},\quad\text{(A6)}$$

where the divergence of the heat flux $\mathbf{h}$ appears in the right-hand side. Applying the CG operation we find

$$\partial_t\overline{\mathcal{E}^{\rm th}}+\nabla\cdot\left(\overline{v\mathcal{E}^{\rm th}}+\bar{\mathbf{h}}\right)=-\bar{\boldsymbol{P}}\colon\nabla\bar{\mathbf{v}}-\left(\overline{\boldsymbol{P}\colon\nabla\mathbf{v}}-\bar{\boldsymbol{P}}\colon\nabla\bar{\mathbf{v}}\right),\quad\text{(A7)}$$

where we find the spatial flux of thermal energy $\mathcal{F}^{\rm th}_\ell=\overline{v\mathcal{E}^{\rm th}}$, the filtered heat flux $\bar{\mathbf{h}}=\mathbf{h}*G_\ell$, the cascade of thermal energy across scale ℓ, $\phi_\ell=(\overline{\boldsymbol{P}\colon\nabla\mathbf{v}}-\bar{\boldsymbol{P}}\colon\nabla\bar{\mathbf{v}})$.

As a conclusion we want to mention a caveat: the careful reader may notice that there is a certain freedom in separating the terms into spatial fluxes or cascades as one can always turn one into the other using an integration by parts. The criteria we followed (which constrain the equations in this form) were mentioned above: no cascading mechanism should appear in Maxwell's equation and that in the limiting case $\mathbf{E}=\mathbf{B}=0$ we should recover the hydrodynamic limit where the terms have been carefully arranged according to their physical meaning (see Aluie [37]).

Appendix B: Turbulent intervals identification.—The pipeline follows with minor modifications the procedure outlined in Stawarz *et al.* [63].

To identify suitable turbulence events we check, between October 2015 and May 2018, for intervals with continuous burst data available. We remove intervals with sharp jumps in the plasma parameters or with crossing of boundaries. We also exclude events in which large scale inhomogeneities are present; for instance, we avoid large scale density gradients and large scale variation of the angle $\theta_{\mathbf{vB}}$ between the flow and the magnetic field.

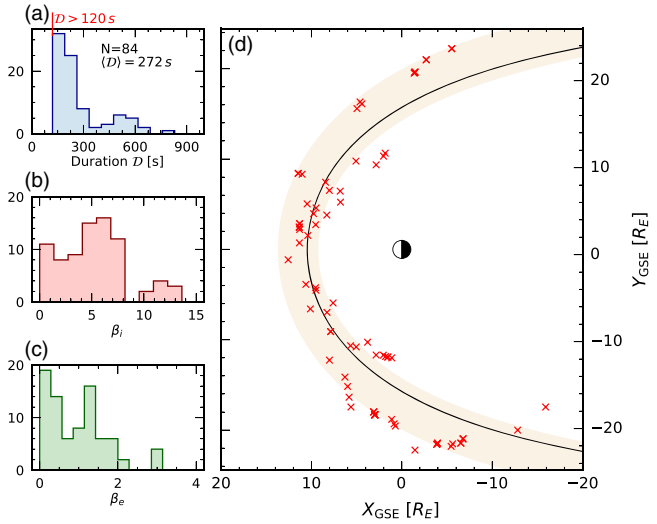

FIG. 5. Panels (a)–(c) Histogram of the intervals duration, ion, and electron plasma β. (d) The location in the plane $X_{\rm GSE}-Y_{\rm GSE}$ of each magnetosheath turbulence interval examined in this study. The shaded region and the continuous line denote the probable magnetopause location based on the Shue model [66].

Following [63] we check the stability of the magnetic correlation scale over different length subintervals and the applicability of the Taylor hypothesis.

We avoid intervals for which the magnetic field spectrum only displays a shallow "f^{-1} range" [64] instead of the usual inertial range.

We then compute the elongation E and planarity P [65] of the tetrahedron formation and only retain intervals for which $\sqrt{E^2+P^2}<0.6$ to avoid configurations that are too distorted. As a last step we discard intervals shorter than 120 s. As a general rule, with the aim of increasing the statistics, we favor having a larger number of shorter intervals (e.g., 180–200 s) rather than having one single longer event (>10 min). Figure 5 displays some features of the dataset used in this work.

Appendix C: Statistics of the cascade rate.—We estimate the value of the energy cascade rate in Earth's magnetosheath at different scales: the small-scale edge of the MHD range $k\rho_i=0.2$, around the ion scale $k\rho_i=2$ and at the subion scale $k\rho_i=10$. Histograms of the cascade rate at different scales are displayed in Fig. 6. To provide a statistically significant measure we identify the minimum number of consecutive logarithmically spaced bins containing over 60% of the dataset. Figure 6(a) shows that MHD scales generally exhibit a cascade rate in the interval $[0.3\text{–}1.4]\times10^{-2}$ nW/m^3, comparable with the values reported in [17,19] using third order laws in Earth's magnetosheath. Notably, this

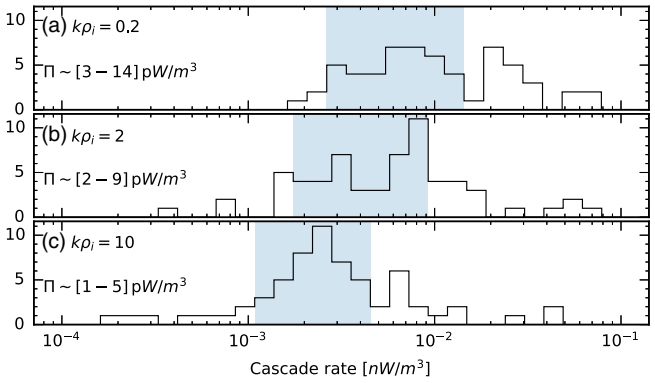

FIG. 6. Histogram of the cascade rate at different scales, $k\rho_i = 0.2$, 2, 10, respectively. The shaded blue region denotes the minimum number of contiguous bins that contains 60% of the dataset.

rate diminishes by a factor of 2 upon reaching $k\rho_i = 2$ [Fig. 6(b)] and further weakens by an additional factor of two at $k\rho_i = 10$ [Fig. 6(c)] reaching a rate in the range $[0.1–0.5] \times 10^{-2}$ nW/m^3. This shows that the subion range is weakly dissipative and that at $k\rho_i \sim 10$ a significant ratio (∼30%) of the cascade rate at MHD scales remains available to sustain the turbulence cascade all the way down to electron scales [51].

Appendix D: MMS event on 23 February 2016.—In Fig. 7, we present the data from MMS3 for (2016/02/23, 20:02:35–20:04:44), corresponding to the magnetic energy spectrum displayed in Fig. 1.

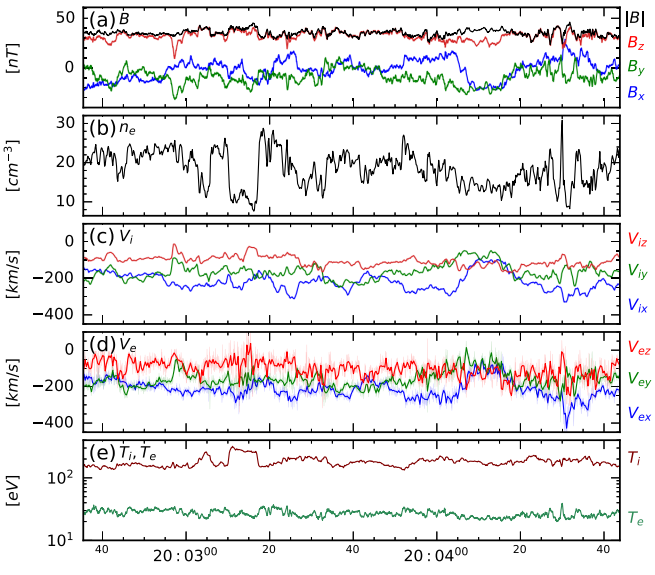

FIG. 7. MMS3 data: (a) the magnetic field in GSE, the electron density (b), ion and electron velocity (c)–(d), ion and electron temperatures (e). In panel (d) we overplot the electron velocity interpolated to the ion time resolution to improve the visualization.

*davide.manzini@lpp.polytechnique.fr

[1] H. Politano and A. Pouquet, Phys. Rev. E **57**, R21 (1998).
[2] F. Sahraoui, L. Hadid, and S. Huang, Rev. Mod. Phys. **4**, 4 (2020).
[3] S. Banerjee and S. Galtier, Phys. Rev. E **87**, 013019 (2013).
[4] N. Andrés, S. Galtier, and F. Sahraoui, Phys. Rev. E **97**, 013204 (2018).
[5] S. Galtier, Phys. Rev. E **77**, 015302(R) (2008).
[6] P. Hellinger, A. Verdini, S. Landi, L. Franci, and L. Matteini, Astrophys. J. Lett. **857**, L19 (2018).
[7] R. Ferrand, S. Galtier, F. Sahraoui, R. Meyrand, N. Andrés, and S. Banerjee, Astrophys. J. **881**, 50 (2019).
[8] P. Simon and F. Sahraoui, Astrophys. J. **916**, 49 (2021).
[9] P. Simon and F. Sahraoui, Phys. Rev. E **105**, 055111 (2022).
[10] L. Sorriso-Valvo, R. Marino, V. Carbone, A. Noullez, F. Lepreti, P. Veltri, R. Bruno, B. Bavassano, and E. Pietropaolo, Phys. Rev. Lett. **99**, 115001 (2007).
[11] B. T. MacBride, C. W. Smith, and M. A. Forman, Astrophys. J. **679**, 1644 (2008).
[12] J. E. Stawarz, C. W. Smith, B. J. Vasquez, M. A. Forman, and B. T. MacBride, Astrophys. J. **697**, 1119 (2009).
[13] J. E. Stawarz, C. W. Smith, B. J. Vasquez, M. A. Forman, and B. T. MacBride, Astrophys. J. **713**, 920 (2010).
[14] J. T. Coburn, C. W. Smith, B. J. Vasquez, J. E. Stawarz, and M. A. Forman, Astrophys. J. **754**, 93 (2012).
[15] S. Banerjee, L. Z. Hadid, F. Sahraoui, and S. Galtier, Astrophys. J. Lett. **829**, L27 (2016).
[16] L. Z. Hadid, F. Sahraoui, and S. Galtier, Astrophys. J. **838**, 9 (2017).
[17] L. Z. Hadid, F. Sahraoui, S. Galtier, and S. Y. Huang, Phys. Rev. Lett. **120**, 055102 (2018).
[18] R. Bandyopadhyay, A. Chasapis, R. Chhiber, T. N. Parashar, W. H. Matthaeus, M. A. Shay, B. A. Maruca, J. L. Burch, T. E. Moore, C. J. Pollock, B. L. Giles, W. R. Paterson, J. Dorelli, D. J. Gershman, R. B. Torbert, C. T. Russell, and R. J. Strangeway, Astrophys. J. **866**, 106 (2018).
[19] N. Andrés, F. Sahraoui, S. Galtier, L. Z. Hadid, R. Ferrand, and S. Y. Huang, Phys. Rev. Lett. **123**, 245101 (2019).
[20] R. Bandyopadhyay, L. Sorriso-Valvo, A. Chasapis, P. Hellinger, W. H. Matthaeus, A. Verdini, S. Landi, L. Franci, L. Matteini, B. L. Giles, D. J. Gershman, T. E. Moore, C. J. Pollock, C. T. Russell, R. J. Strangeway, R. B. Torbert, and J. L. Burch, Phys. Rev. Lett. **124**, 225101 (2020).
[21] N. Andrés, F. Sahraoui, L. Z. Hadid, S. Y. Huang, N. Romanelli, S. Galtier, G. DiBraccio, and J. Halekas, Astrophys. J. **919**, 19 (2021).
[22] M. Brodiano, P. Dmitruk, and N. Andrés, Phys. Plasmas **30**, 032903 (2023).
[23] F. Pecora, Y. Yang, W. H. Matthaeus, A. Chasapis, K. G. Klein, M. Stevens, S. Servidio, A. Greco, D. J. Gershman, B. L. Giles, and J. L. Burch, Phys. Rev. Lett. **131**, 225201 (2023).
[24] M. Germano, J. Fluid Mech. **238**, 325 (1992).
[25] G. L. Eyink, Physica (Amsterdam) **207D**, 91 (2005).
[26] H. Aluie, New J. Phys. **19**, 025008 (2017).
[27] E. Camporeale, L. Sorriso-Valvo, F. Califano, and A. Retinò, Phys. Rev. Lett. **120**, 125101 (2018).
[28] S. S. Cerri and E. Camporeale, Phys. Plasmas **27**, 082102 (2020).

[29] Y. Yang, W. H. Matthaeus, T. N. Parashar, C. C. Haggerty, V. Roytershteyn, W. Daughton, M. Wan, Y. Shi, and S. Chen, Phys. Plasmas **24**, 072306 (2017).
[30] D. Manzini, F. Sahraoui, F. Califano, and R. Ferrand, Phys. Rev. E **106**, 035202 (2022).
[31] D. Manzini, F. Sahraoui, and F. Califano, Phys. Rev. Lett. **130**, 205201 (2023).
[32] S. Adhikari, Y. Yang, W. H. Matthaeus, P. A. Cassak, T. N. Parashar, and M. A. Shay, arXiv:2310.16973.
[33] G. Belmont, R. Grappin, F. Mottez, F. Pantellini, and G. Pelletier, *Collisionless Plasmas in Astrophysics* (Wiley, New York, 2013), p. 119.
[34] R. Fitzpatrick, *Plasma Physics. An Introduction* (CRC Press, Boca Raton, 2022).
[35] The interested reader can find more details on properties and effect of different filtering functions in Manzini *et al.* [30] and references therein.
[36] H. Aluie, Phys. Rev. Lett. **106**, 174502 (2011).
[37] H. Aluie, Physica (Amsterdam) **247D**, 54 (2013).
[38] G. G. Howes, K. G. Klein, and T. C. Li, J. Plasma Phys. **83**, 705830102 (2017).
[39] R. Ferrand, F. Sahraoui, D. Laveder, T. Passot, P. L. Sulem, and S. Galtier, Astrophys. J. **923**, 122 (2021).
[40] J. L. Burch, T. E. Moore, R. B. Torbert, and B. L. Giles, Space Sci. Rev. **199**, 5 (2016).
[41] G. Chanteur, in *ISSI Scientific Report Book: Analysis Methods for Multi-Spacecraft Data*, ISSI Scientific Reports Series SR-001, ESA/ISSI Vol. 1 (1998), Chap. 14, ISBN 1608-280X.
[42] P.-A. Lindqvist, G. Olsson, R. B. Torbert, B. King, M. Granoff *et al.*, Space Sci. Rev. **199**, 137 (2016).
[43] R. E. Ergun, S. Tucker, J. Westfall, K. A. Goodrich, D. M. Malaspina *et al.*, Space Sci. Rev. **199**, 167 (2016).
[44] C. Pollock, T. Moore, A. Jacques, J. Burch, U. Gliese *et al.*, Space Sci. Rev. **199**, 331 (2016).
[45] D. J. Gershman, J. C. Dorelli, L. A. Avanov, U. Gliese, A. Barrie, C. Schiff, D. E. Da Silva, W. R. Paterson, B. L. Giles, and C. J. Pollock, J. Geophys. Res. **124**, 10345 (2019).
[46] O. W. Roberts, Z. Vörös, K. Torkar, J. Stawarz, R. Bandyopadhyay, D. J. Gershman, Y. Narita, R. Kieokaew, B. Lavraud, K. Klein, Y. Yang, R. Nakamura, A. Chasapis, and W. H. Matthaeus, J. Geophys. Res. **128**, e2023JA031565 (2023).
[47] P. Welch, IEEE Trans. Audio Electroacoust. **15**, 70 (1967).
[48] P. Hellinger, V. Montagud-Camps, L. Franci, L. Matteini, E. Papini, A. Verdini, and S. Landi, Astrophys. J. **930**, 48 (2022).
[49] Y. Yang, W. H. Matthaeus, S. Roy, V. Roytershteyn, T. N. Parashar, R. Bandyopadhyay, and M. Wan, Astrophys. J. **929**, 142 (2022).
[50] S. Roy, R. Bandyopadhyay, Y. Yang, T. N. Parashar, W. H. Matthaeus, S. Adhikari, V. Roytershteyn, A. Chasapis, H. Li, D. J. Gershman, B. L. Giles, and J. L. Burch, Astrophys. J. **941**, 137 (2022).
[51] F. Sahraoui, M. L. Goldstein, P. Robert, and Y. V. Khotyaintsev, Phys. Rev. Lett. **102**, 231102 (2009).
[52] G. G. Howes, J. M. TenBarge, W. Dorland, E. Quataert, A. A. Schekochihin, R. Numata, and T. Tatsuno, Phys. Rev. Lett. **107**, 035004 (2011).
[53] D. Told, F. Jenko, J. M. TenBarge, G. G. Howes, and G. W. Hammett, Phys. Rev. Lett. **115**, 025003 (2015).
[54] F. Sahraoui, M. L. Goldstein, G. Belmont, P. Canu, and L. Rezeau, Phys. Rev. Lett. **105**, 131101 (2010).
[55] A. A. Schekochihin, J. T. Parker, E. G. Highcock, P. J. Dellar, W. Dorland, and G. W. Hammett, J. Plasma Phys. **82**, 905820212 (2016).
[56] S. Servidio, A. Chasapis, W. H. Matthaeus, D. Perrone, F. Valentini, T. N. Parashar, P. Veltri, D. Gershman, C. T. Russell, B. Giles, S. A. Fuselier, T. D. Phan, and J. Burch, Phys. Rev. Lett. **119**, 205101 (2017).
[57] O. Pezzi, S. Servidio, D. Perrone, F. Valentini, L. Sorriso-Valvo, A. Greco, W. H. Matthaeus, and P. Veltri, Phys. Plasmas **25**, 060704 (2018).
[58] P. A. Cassak, M. H. Barbhuiya, H. Liang, and M. R. Argall, Phys. Rev. Lett. **130**, 085201 (2023).
[59] C. H. K. Chen, K. G. Klein, and G. G. Howes, Nat. Commun. **10**, 740 (2019).
[60] A. S. Afshari, G. G. Howes, C. A. Kletzing, D. P. Hartley, and S. A. Boardsen, J. Geophys. Res. **126**, e2021JA029578 (2021).
[61] A. Jeandet and A. Schulz, *Speasy: Space physics made easy* (2022), https://zenodo.org/doi/10.5281/zenodo.4118780.
[62] V. Génot, E. Budnik, C. Jacquey, M. Bouchemit, B. Renard, N. Dufourg, N. André, B. Cecconi, F. Pitout, B. Lavraud *et al.*, Planet. Space Sci. **201**, 105214 (2021).
[63] J. E. Stawarz, J. P. Eastwood, T. D. Phan, I. L. Gingell, P. S. Pyakurel, M. A. Shay, S. L. Robertson, C. T. Russell, and O. Le Contel, Phys. Plasmas **29**, 012302 (2022).
[64] S. Y. Huang, L. Z. Hadid, F. Sahraoui, Z. G. Yuan, and X. H. Deng, Astrophys. J. Lett. **836**, L10 (2017).
[65] G. Paschmann and P. W. Daly, in *ISSI Scientific Report Book: Analysis Methods for Multi-Spacecraft Data*, ISSI Scientific Reports Series SR-001, ESA/ISSI Vol. 1 (1998), Chap. 13, ISBN 1608-280X.
[66] J.-H. Shue, P. Song, C. T. Russell, J. T. Steinberg, J. K. Chao, G. Zastenker, O. L. Vaisberg, S. Kokubun, H. J. Singer, T. R. Detman, and H. Kawano, J. Geophys. Res. **103**, 17691 (1998).